

Topological learning for the classification of disorder: an application to the design of metasurfaces

Tristan Madeleine,^{*,†} Nina Podoliak,[‡] Oleksandr Buchnev,[¶] Ingrid Membrillo Solis,[†] Giampaolo D'Alessandro,[†] Jacek Brodzki,[†] and Malgosia Kaczmarek[‡]

[†]*Mathematical Sciences, University of Southampton, Southampton SO17 1BJ, United Kingdom*

[‡]*Physics and Astronomy, University of Southampton, Southampton SO17 1BJ, United Kingdom*

[¶]*Optoelectronics Research Centre and Centre for Photonic Metamaterials, University of Southampton, Southampton SO17 1BJ, UK*

E-mail: tm3u18@soton.ac.uk

Abstract

Structural disorder can improve the optical properties of metasurfaces, whether it is emerging from some large-scale fabrication methods, or explicitly designed and built lithographically. Correlated disorder, induced by a minimum inter-nanostructure distance or by hyperuniformity properties, is particularly beneficial in some applications such as light extraction. We introduce numerical descriptors inspired from topology to provide quantitative measures of disorder whose universal properties make them suitable for both uncorrelated and correlated disorder, where statistical descriptors are less accurate. We prove theoretically and experimentally the accuracy of these

topological descriptors of disorder by using them to design plasmonic metasurfaces of controlled disorder, that we correlate to the strength of their surface lattice resonances. These tools can be used for the fast and accurate design of disordered metasurfaces, or to help tuning large-scale fabrication methods.

Abbreviations

SLR,TDA

Keywords

Metasurface, Surface lattice resonance, topological data analysis, plasmonic, disorder, design, optimisation

Metasurfaces are two-dimensional metamaterials with subwavelength scattering elements designed to have electromagnetic properties unobtainable from bulk materials.¹ However, their designs usually require expensive and time consuming fabrication methods, such as lithography, limiting their large-scale and large surface area production. In order to circumvent these limitations, extensive work is being conducted to devise quicker and less expensive fabrication methods for large-scale metasurfaces, usually at the cost of emerging structural disorder. Some examples are gas-phase cluster beam deposition,² nanosphere photolithography³ or lithography free fabrication methods,⁴ such as bottom up self assembled systems,⁵⁻⁹ colloid deposition¹⁰ or polymer phase separation.¹¹⁻¹³

While the emergence of structural disorder is usually thought as being an unavoidable downside of these fabrication methods, some photonic based applications actually benefit from it.¹⁴ Indeed positional disorder helps to tune¹⁵⁻¹⁷ or reduce the diffraction,¹⁸ scattering,¹⁹ reflection^{6,8} or radiation^{17,20} of metasurfaces, with potential applications in the fabrication of better displays.²¹ Disorder can also suppress grating effects²², make surface-enhanced Raman scattering broadband,¹¹ enhance localised photoluminescence,²³ improve

wavefront shaping,^{24,25} improve light absorption,^{26,27} e.g. for solar cells,¹² or light extraction.^{5,28} For example, coating the air-LED interface with disordered nanostructures provides a broadband coupling between what would have been internally trapped photons to the external radiation, making more energy efficient LEDs.² In some of these fields, correlated disorder seems to be particularly important. Indeed, a correlation length, either induced by a minimum distance between the nanostructures, or by some stealthy hyperuniformity properties helps to create metasurfaces with broader absorption bands,²⁶ broader diffusive properties¹⁹ or prevent light trapping between nanostructures for more efficient light extraction.²⁸

The different applications of disordered metasurfaces lead to more recent effort to tailor disorder for specific desired optical properties,²⁹⁻³² for example using inverse design methods^{33,34} based on machine learning^{35,36} or via topology optimisation.^{37,38} Indeed, combining disorder engineering and topology optimisation one can build metasurfaces with selective light polarisation conversion while minimising the in-plane phase fluctuation.³⁹ While these methods directly generate optimised disordered patterns, they can be time consuming and computationally expensive to implement. In some cases, knowing the link between disorder and the optical properties of a metasurface could significantly speed up the design process by restricting the optimisation to the degree of disorder of a metasurface. However, despite many methods existing to quantify disorder, they all have their strength and weaknesses and are only relevant for specific applications.³² In this work, we present new topology inspired numerical tools suitable for the characterisation of disordered metasurfaces. Their universality makes them useful for the characterisation of both correlated and uncorrelated disorder, and can be used either for the characterisation of disordered metasurfaces built with techniques similar to those mentioned above, or for the fast and accurate design of metasurfaces of specific disorder levels. We demonstrate the relevance of these tools by designing and fabricating metasurfaces made of plasmonic nanostructures embedded in dielectric media whose structural correlated disorder is related to the strength of their surface

lattice resonances (SLR).

Results and discussion

We first present a generalised model of disorder generation. We show that a large correlation length may lead to potentially ambiguous designs, where the degree of disorder is poorly represented by the generative/statistical parameters, hinting to the need for better disorder descriptors. We then introduce the field of Topological Data Analysis (TDA) and the tools required to characterise metasurfaces. Using them, we show that correlated disordered metasurfaces are poorly represented by their generative parameters, while being suitably described by these topological descriptors. We then prove the characterisation accuracy and predictive properties of these tools by designing metasurfaces with specific disorder levels, first theoretically then experimentally.

Models of correlated and uncorrelated disorder

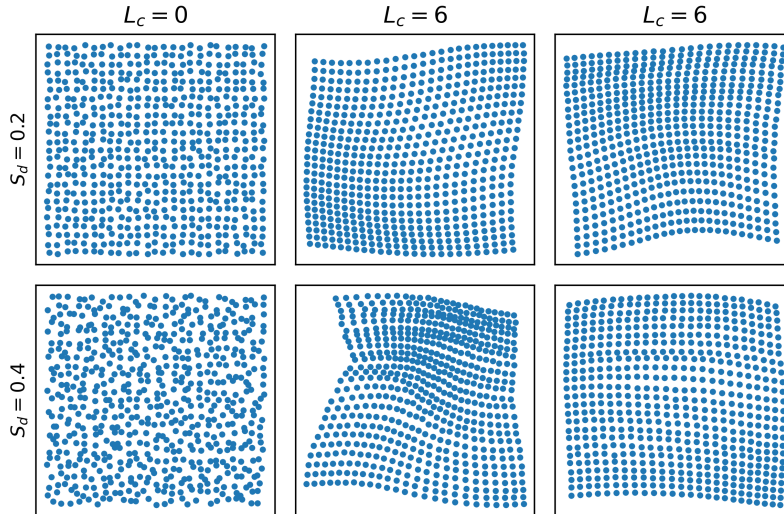


Figure 1: Examples of generated disordered lattices. The top row corresponds to lattices generated with $S_d=0.2$ and the bottom row correspond to lattices generated with $S_d=0.4$. The left column represents uncorrelated disordered lattices, $L_c=0$, while the middle and right column represents correlated disordered lattices, $L_c=6$.

A recent work¹⁷ presented a model of disorder to study how correlated and uncorrelated disorder influences the far-field optical response of a metasurface. We apply our characterisation of disorder on their model that we reintroduce here.

Starting with a regular lattice, such as a square lattice of period P made of $N_x \times N_y = N$ nanostructures whose positions are defined by $\vec{r}_i, i \in [1, N]$, we can define correlated and uncorrelated disorder as follows. Each nanostructure position is modified by a random vector $\vec{\Delta r}_i$ whose x and y components are generated from a continuous uniform probability distribution bounded by $[-S_d P, S_d P]$. The non dimensional parameter S_d determines the strength of the uncorrelated disorder. A correlation length can be implemented by adding to $\vec{\Delta r}_i$ the uncorrelated disorder of nearby nanostructures, indexed by j , weighted according to how far they are with a factor C_{ij} ,

$$C_{ij} = e^{-\left(\frac{r_{ij}}{2L_c P}\right)^2}, \quad (1)$$

with r_{ij} the distance between the nanostructure i and j , including the uncorrelated disorder applied to \vec{r}_i and \vec{r}_j . The correlation length is given by the full width at half maximum of C_{ij} which is equal to $2\sqrt{2 \ln 2} L_c P$, which is proportional to the non dimensional parameter L_c . The total disorder perturbation can be summarised as:

$$\vec{r}'_i = \vec{r}_i + \vec{\Delta r}_i + \sum_{j \neq i} \vec{\Delta r}_j C_{ij}. \quad (2)$$

Using the expression (2), we generated lattices with varying values of L_c and S_d , see figure 1. On the left column of figure 1, one can visually appreciate that the strength of uncorrelated disorder, for $L_c=0$, is well represented by S_d . Adding a correlation length, for example in the middle and right columns of figure 1 makes the lattices' distortion smoother. However, if one can still guess that the middle column, bottom lattice is more disordered than the middle column, top lattice, as they were respectively generated with $S_d=0.4$ and $S_d=0.2$, this is not systematically the case. Indeed, the lattices in the right column were generated

with the same parameters L_c and S_d as in the middle column, however the relative disorder strength of these two lattices is ambiguous.

While a correlation length makes the generative parameter S_d less accurate to represent the positional disorder of a lattice, it also destroys the information about the original regular lattice by inducing collective movements of the lattice's points. This makes a statistical description of correlated disordered lattices much harder due to not having a reference lattice to compare them to. In order to circumvent these constraints, we introduce topology inspired numerical tools allowing to compare lattices with each other in a way that highlights the influence of a correlation length and provides a more accurate measure of disorder than S_d .

Topological characterisation of disorder

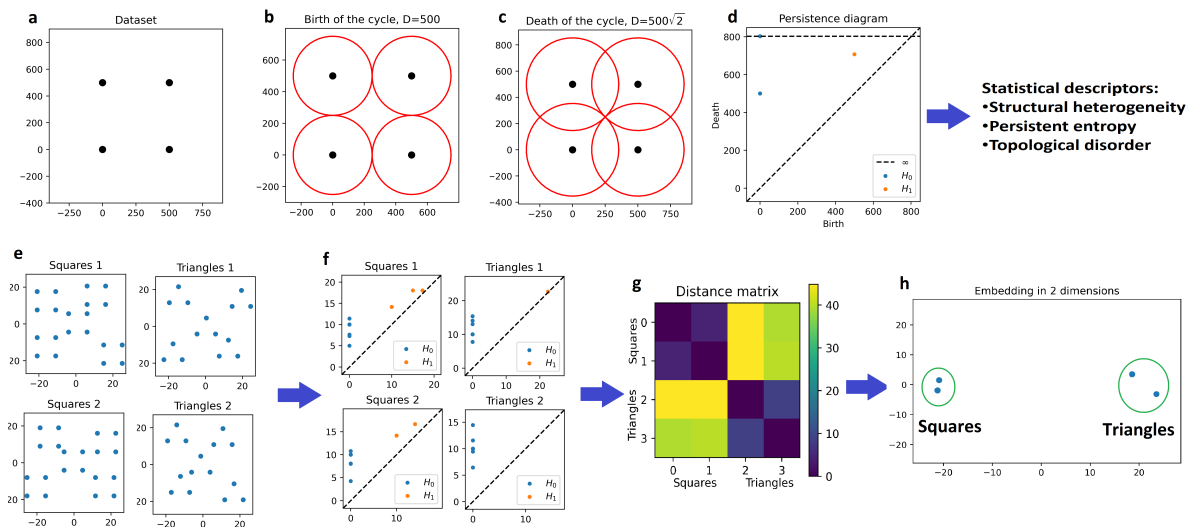


Figure 2: Examples of two key TDA process used in this paper. The top row represents the computation of persistent homology from the dataset (a) to its representation in a persistent diagram (d). In (b) and (c) are represented the circles whose diameters correspond respectively to the birth and death of the loop of this dataset (single H_1 point in the persistence diagram in panel d). The bottom row represents the computation of the embedding of datasets (e) in a two dimensional space (h) via the computation of their persistence diagrams (f) and the distance between them (g). Datasets of the same type are clustered in the embedding space (panel h).

Topological Data Analysis (TDA) is a collection of tools inspired from topology and ge-

ometry designed to provide qualitative and quantitative descriptors of structures in datasets. It has had various applications in different fields ranging from cosmology^{40,41} to solid state physics.^{42–46} One of its sub-fields, persistent homology, is particularly efficient to recover the scale of topological features. We provide here a brief description of the procedure. Interested readers can find detailed introductory notes^{47,48} and the whole process can be executed using standard libraries such as GUDHI⁴⁹ or Ripser.⁵⁰

Starting from a point cloud such as that in panel a of figure 1, we build a collection of topological spaces called Rips simplicial complexes, indexed by a real number r . For a given value of r , the complex is constructed as follows. A ball of radius r is drawn around each point of the point cloud. If two balls intersect, we add a link between their respective centres. Similarly, higher order links are added to the complex upon the intersection of three or more balls. Restricting ourselves to only two dimensions, which is relevant for flat metasurfaces, we draw circles of radius r around each point and we only consider connections between pairs and triplets of points. The topological properties of each simplicial complex, the number of connected components and the number of loops in two dimensions, can be directly computed using algebraic topology. Tracking the evolution of these topological features for different values of r provide useful insight over their scale. These features can be summarise in a persistence diagram for which each feature, indexed by the integer i , is represented by two coordinates, their "birth", b_i and their "death", d_i , which are the values of $2r$ at which they appear and disappear.

For example, if we consider a simple point cloud such as a square of side 500 in figure 2a, we see the birth of a loop when the diameter of the circles is equal to the side length of the square, figure 2b. This loop dies when the diameter is equal to the diagonal of the square, figure 2c, and the birth and death of this loop is represented as the point at coordinates (500, 707) in a persistence diagram, figure 2d. Additionally, four connected components are born at $r = 0$ and three of them die such that only one remains after the circles intersect in figure 2b. Therefore, three (overlapping) points at coordinates (0, 500) are represented

in figure 2d. The last connected components remains for $r \rightarrow \infty$. As we stopped the computation of persistent homology at $r = 400$ we assign to this point coordinates $(0, 800)$.

The second row of figure 3 illustrates how TDA can be used for the clustering analysis of point clouds. The first step is to measure the “distance” between point clouds (figure 3e). We do this by measuring the distance between their corresponding persistence diagrams. Several metrics can be defined over the space of the persistence diagrams and we have selected to use the Wasserstein distance⁵¹ for its simplicity of use (figure 3f and 3g). If several point clouds are considered, one can build a geometrical embedding, for example via classical multidimensional scaling,⁵² in which each point cloud can be represented as one point and the distance between each point is given by the distance between their respective persistence diagrams (figure 3h). This provides a visual representation of the configuration space of the different point clouds and can be used to detect clustering. For example, we considered two sets of four point clouds made of either triangles or squares, such as represented in figure 2e. Upon computing their persistence diagrams, figure 2f, and the distance matrix between them, figure 2g, we observe that a square seems to be more similar, or closer, to the other square than to the triangles. This can be directly visualised in their embedding in figure 2h, where we observe two clusters corresponding to the sets of squares and triangles.

In order to visualise the space of configurations obtained from the definition of correlated disordered lattices in (2), we performed the embedding of 1203 lattices generated for three different lattice periods, 500, 600 and 700 nm, and five different values of $S_d \in [0, 0.4]$. We repeated this for uncorrelated disorder, $L_c=0$, weakly correlated disorder, $L_c=2$, and strongly correlated disorder, $L_c=8$ (panels a,b and c of figure 3). We see in figure 3a an unambiguous clustering of the uncorrelated disorder lattices generated with the same parameters, i.e. S_d and the original lattice period. For a fixed value of the period, the lattices appear to live on a simple curve on which we see five separated clusters of points corresponding to the five values of S_d considered. As can be seen in figure 3b, a correlation length increases the size of each cluster, allowing them to overlap. For a large correlation length, like in figure 3c, each cluster

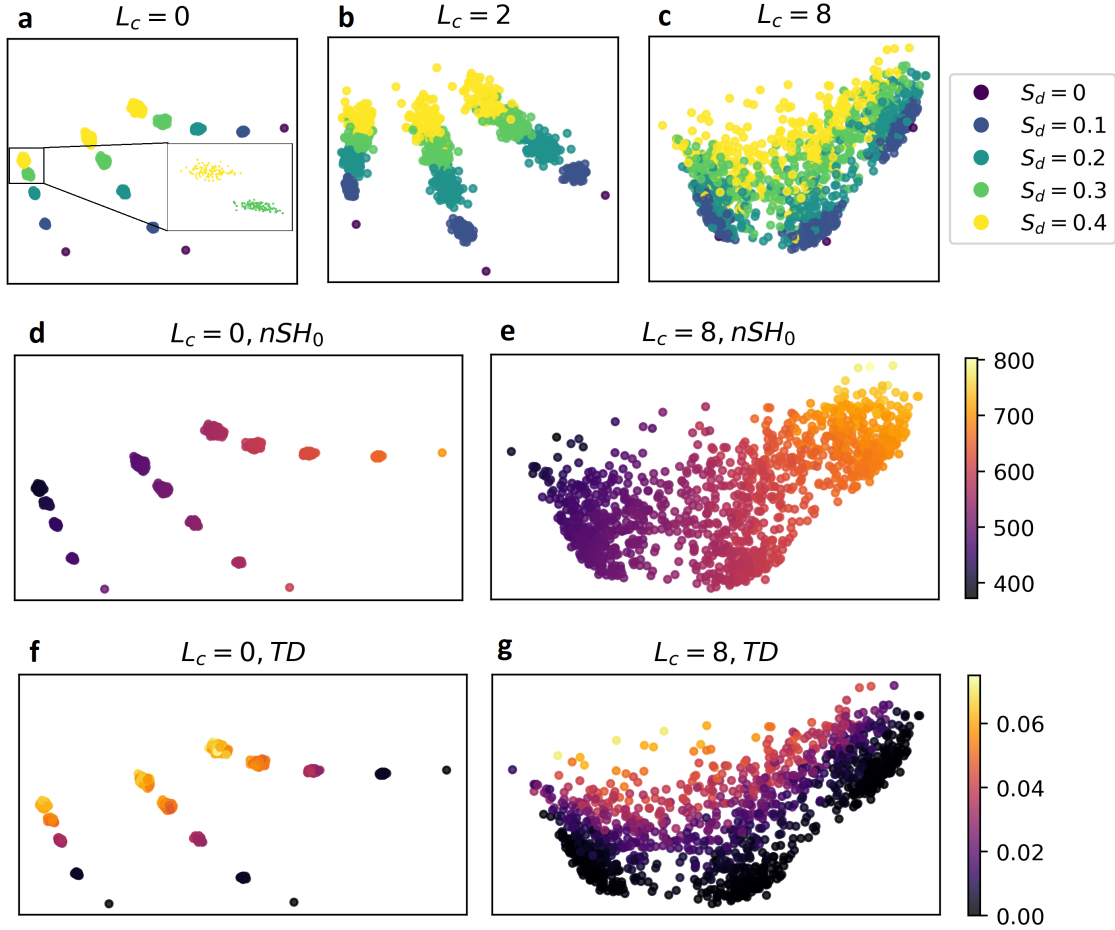


Figure 3: Scatter plots of the two dimensional embedding of three sets of generated lattices with uncorrelated (a), weakly correlated (b) and strongly correlated (c) disorder. Each set was generated from an original square lattice of period 500, 600 and 700 nm (left to right in panel a) and with $S_d \in [0, 0.4]$. In the absence of correlation, lattices with different values of the period and of S_d are well clustered. In the insert of panel a we adapted the size of points to illustrate how clustered the lattices are. The clustering is lost in the presence of correlations, panels b and c. Panels d and f, and panels e and g are equivalent to panels a and c respectively, with colour coding based on the value of nSH_0 (TD) in panels d and f (e and g). In both cases the colour gradient is not significantly affected by correlation.

is so large that they form one common cluster between the three different periodicities and the different values of S_d . This is in agreement with what we presented in the previous section. A non-zero correlation length allows the lattices to explore a broader configuration space. Therefore, one can generate lattices that are more different from each other despite using the same parameters and the overall size of the clusters, related to the maximum distance between the persistence diagrams of the generated lattices, is bigger. This expansion of the lattices configuration space leads to situations where two lattices generated with different parameters may actually be very similar to each other, which is represented by the overlap between the clusters in figure 3b. Eventually, a large enough correlation length will make the clusters big enough to make the generative parameters obsolete, which is what we observe in figure 3c. Indeed, even if one can see some general trend between the overall lattices position and the value of S_d , one cannot accurately recover the value of S_d based on the lattice position. This can lead to situations where a lattice generated with a high amount of disorder, i.e. a large value of S_d , may be as, or more, ordered than a lattice generated with a small amount of disorder, such as represented in the right column of figure 1.

Using TDA, we were able to show the limitation of the parameter S_d to characterise generated lattices. One can build several metrics to describe persistence diagrams, which can be used as simpler descriptors of the topology of datasets, or as inputs of more refined machine learning based models.^{53,54} In this work, we use two statistical descriptors based on lattices' persistence diagrams in order to describe both the typical distance between each point of the lattices and their positional disorder. The first numerical descriptor is normalised structural heterogeneity of degree 0 (nSH_0) and is the sum of the lifetime of the topological features of degree 0, the connected components,⁵⁵ divided by the number of points of the lattice, N :

$$nSH_0 = \frac{1}{N} \sum_{(b,d) \in H_0 \subset \mathfrak{D}} d - b, \quad (3)$$

with b and d the birth and death of each topological feature of degree 0, H_0 , of the persistence diagram \mathfrak{D} . As the death of the topological features of degree 0 is proportional to the

distance between the points of the lattices, nSH_0 can be directly related to the average nearest neighbour distance between the nanostructures. If we colour the embeddings of uncorrelated and strongly correlated, $L_c=8$, lattices of figure 2 according to the value of nSH_0 of each lattice, we see in figure 2d that this quantity almost recovers perfectly the periodicity of the lattice for uncorrelated disorder, which confirms our interpretation of the topological features of degree 0. When applied to strongly correlated disordered lattices, figure 2e, SH_0 provides a smooth ordering of the lattices, following a similar trend as for uncorrelated disordered lattices.

We also introduce a new descriptor that we call Topological Disorder (TD), inspired from the persistent entropy (PE).^{56–58} PE is defined as

$$PE = - \sum_{(b,d) \in \mathfrak{D}} \frac{d-b}{L} \ln \left(\frac{d-b}{L} \right), \quad L = \sum_{(b,d) \in \mathfrak{D}} d-b. \quad (4)$$

PE is maximal for $d-b = l$ (constant), $\forall (b,d) \in \mathfrak{D}$ and equal to $\log \Omega$, with Ω the total number of topological features in \mathfrak{D} . Therefore, PE is maximal for regular, periodic lattices and measures how ordered lattices are. In order to avoid the counter intuitive association of a highly ordered lattice with its high persistent entropy, and to define a measure of disorder independent of the lattice's size, which modifies the number of topological features Ω , we define TD as

$$TD = \sum_i \left[1 + \frac{\sum_{(b,d) \in H_i \subset \mathfrak{D}} \frac{d-b}{L_i} \ln \left(\frac{d-b}{L_i} \right)}{\log \Omega_i} \right], \quad L_i = \sum_{(b,d) \in H_i \subset \mathfrak{D}} d-b, \quad (5)$$

where we split the computation over the degrees i of the topological features, in order to capture the fundamental differences between topological features of different degree. Indeed, one can see on figure 2d that, despite the regularity of the dataset in figure 2a, the topological features in the persistence diagram are located in different places, which would artificially increase the value of TD . While the example in figure 2a is simple, this remains the case

for ordered lattices. By construction, TD is invariant by rescaling of the typical length of the lattices, making it an orthogonal descriptor of the lattices with respect to nSH_0 . TD is also minimal for ordered lattices, equal to 0, and is independent of the number of points of the lattices. Therefore, it can be used as a universal measure of disorder, not only for point clouds perturbed from different periodic lattices array, but also for point clouds without any inherent order, such as in self-assembled systems. If we colour the embeddings of uncorrelated and strongly correlated lattices of figure 3 according to their TD , we see in figure 3f that TD recovers perfectly the strength of the uncorrelated disorder, regardless of the lattices' periodicity, which confirms that TD is indeed a measure of the lattices' disorder. When applied to strongly correlated disordered lattices, figure 3g, TD provides another smooth ordering of the lattices, orthogonal to the one given by nSH_0 .

These observations suggest that TD and nSH_0 are two topologically inspired descriptors that can be used to quantify the positional disorder and the typical distance between points of a dataset respectively. Being, by construction, independent of any reference dataset, these tools are suitable to classify datasets that are not easily described using classical statistical methods, such as correlated disorder point clouds or self-assembled systems.

Tailored metasurface design, fabrication and spectroscopy

We demonstrate the accuracy of TD by using it to design, and subsequently build, plasmonic metasurfaces of specific degree of disorder, that we relate to the strength of their SLRs. We first investigate the link between TD and the strength of the SLRs theoretically using the discrete dipole approximation.⁵⁹ We randomly generated lattices of 25×25 points with $L_c=8$ and $S_d=0.3$, starting from a square lattice of period 500 nm, where each point represents the position of a plasmonic nanostructure. Filtering the point clouds using nSH_0 , we restrict ourselves to metasurfaces of similar nearest neighbour distance. From these point clouds, we pick those with the highest, lowest and median value of TD (figure 4a, b and c). We consider each nanostructure to be a gold nanocylinder of height 50 nm and diameter 120 nm

whose optical properties, under the dipole approximation, are fully determined by their polarisability. The gold nanocylinders are assumed to be embedded in an homogeneous glass like dielectric layer of refractive index 1.41. We numerically compute the reflectance of the three metasurfaces under illumination by a circularly polarised plane at normal incidence, figure 4d. As predicted, the higher the topological disorder, the weaker the SLRs are. Indeed, we can see on figure 4d that the amplitude of SLR dip is inversely proportional to TD . Similarly, the quality factors of these resonances which are 8.2, 7.5 and 6.5 for the lowest, median and highest TD respectively.

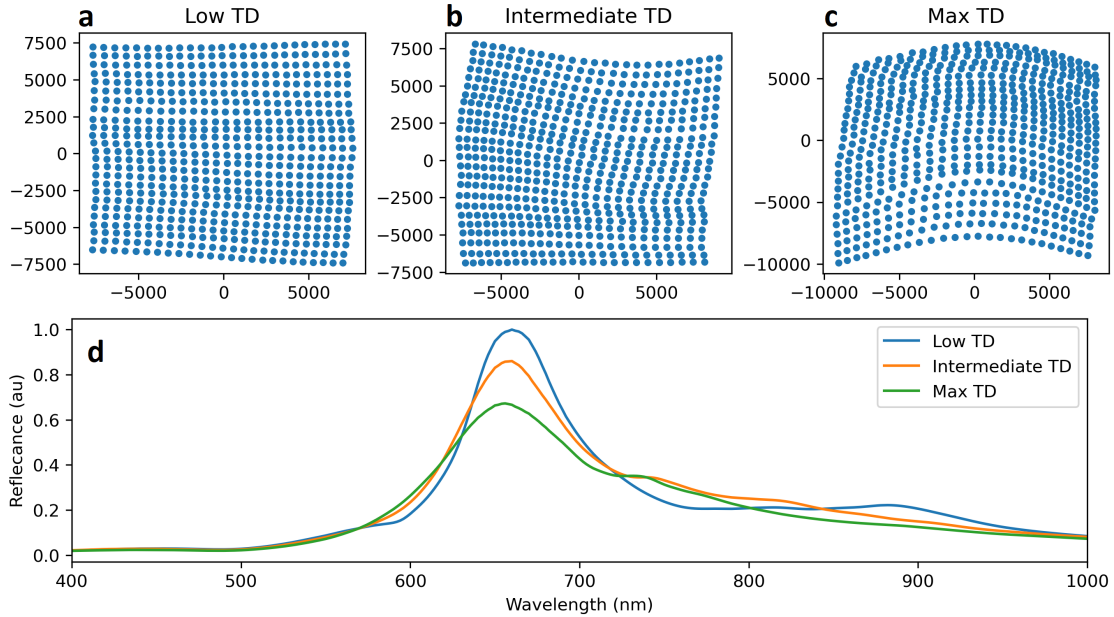


Figure 4: Theoretical investigation of the correlation between TD and the strength of SLR. a,b and c represent respectively the generated metasurfaces of lowest, median and highest TD . Their computed reflectance spectrum, in arbitrary units, is represented in d.

Experimental verification of the TD –SLR link

We additionally experimentally confirmed the link between TD and the strength of SLRs by designing metasurfaces built using Focused Ion Beam (FIB) lithography. Using three different correlation lengths $L_c \in \{6, 8, 10\}$ and starting from a regular square lattice of

period 500 nm, we generated several hundreds of lattices for two values of S_d : 0.2 and 0.4. For each value of L_c , we selected two lattices to compare with each other: the one with the highest value of TD among those generated with $S_d=0.2$ and the one with the lowest value of TD among those generated with $S_d=0.4$. Similarly to the previous section, we used SH_0 to select lattices of similar nearest neighbour distances. We built two sets of seven metasurfaces, three pairs for each value of L_c and one reference square lattice of period 500 nm. The two sets only differ in the size of the nanostructures, which in both cases were elongated 50 nm thick gold nanodisk. The top nanodisk crosssections are elliptical with x - and y -axis of size (160,180) nm and (120,140) nm for the first and second set respectively. The resonant wavelength of the SLRs depends both on the distance between the nanostructures and on their polarisability. The latter is strongly affected by the shape of the nanostructures and their anisotropy induces a shift of the SLRs wavelength of up to 60 nm according to the polarisation of the exciting light. We therefore report the optical properties of the metasurfaces excited under normal incidence light for two linear polarisation: polarised along the y -direction, parallel to the nanostructures' long axis and polarised along the x -direction, perpendicular to the nanostructures' short axis. SEM images of the first set, as well as their transmittance spectrum compared to the square lattice are in figure 5. The results for the second set of metasurfaces, the comparison of these experimental results to the dipolar model and close up SEM images are in the supplementary information.

The three columns of figure 5 contain for each L_c , the SEM images of the designed pair of metasurfaces (first row) and their transmittance spectra upon excitation by light polarised parallel to the nanostructures' long axis (second row) and perpendicular to the nanostructures' short axis (third row). The transmittance spectrum of a periodic metasurface with the same pitch is added for comparison (black lines). We report in table 1 the quality factors of all the SLRs shown in figure 5 as well as the TD of the corresponding metasurfaces.

As can be seen in figure 5 and table 1, in five configurations out of six, the SLRs of the metasurfaces designed with a high S_d but a low TD are stronger and have a larger

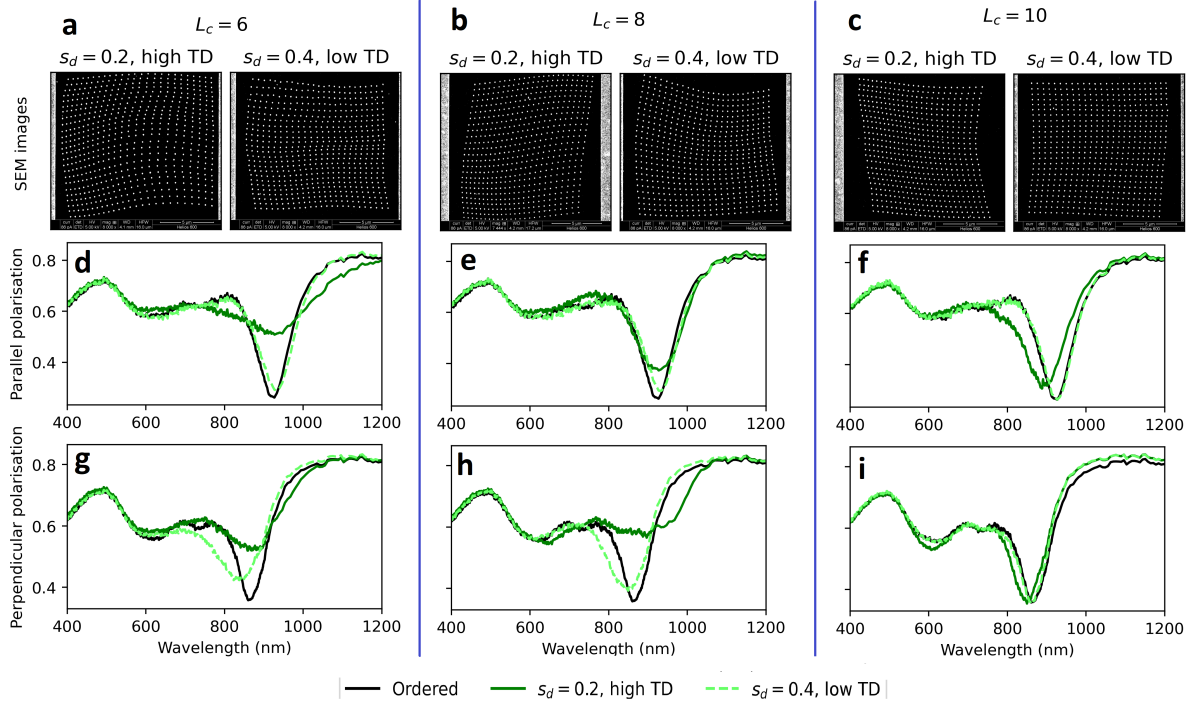


Figure 5: SEM images of the experimental samples (top row) and their transmittance spectra under normal incidence light linearly polarised parallel (middle row) or perpendicular (bottom row) to the long axis of the nanostructures. Each plot displays the spectra of a low and high TD metasurface, dashed pink and solid red respectively, and an ordered metasurface with the same pitch (black). Each column correspond to the metasurfaces generated with $L_c \in [6, 8, 10]$ from left to right.

Table 1: TD of the metasurfaces reported in figure 5 and the corresponding quality factors (Q) of their SLRs for parallel and perpendicular polarisation of the exciting light.

Lattice parameters	TD	Q (parallel)	Q (perpendicular)
$L_c=0, S_d=0$	0.	10.1	11.5
$L_c=6, S_d=0.2$	0.030	4	5.2
$L_c=6, S_d=0.4$	0.012	9.3	6.8
$L_c=8, S_d=0.2$	0.025	6.7	4.4
$L_c=8, S_d=0.4$	0.005	7.8	7
$L_c=10, S_d=0.2$	0.026	8	11.5
$L_c=10, S_d=0.4$	0.002	10.1	11.5

quality factor than the metasurfaces designed with a low S_d but a high TD , proving that TD is indeed an accurate measure of disorder. The only exception is the configuration with $L_c=10$ and perpendicular polarisation, figure 5i, for which both metasurfaces have similarly strong SLRs with a quality factor of 11.5, equivalent to the square lattice for this polarisation. Upon inspecting the lattices of the two metasurfaces generated for $L_c=10$, shown in the panel c of figure 5 or in larger versions in the supplementary information, one can visually appreciate that positional distortion seems to be only noticeable at a large-scale, while at short scales, the nanostructures seem to be more regularly spaced as if they were on a square lattice. Indeed, larger values of L_c average out the uncorrelated disorder of more nearby nanostructures which effectively smooths out the positional shift of each nanostructure, while maintaining large-scale shifts, responsible for the wavy patterns of the two right columns of figure 1. Although TD is able to detect this large-scale distortion, and treats it similarly to short scale disorder, the strength of SLR depends mostly on the latter. Indeed, the interaction strength between the nanostructures decreases as the inverse of the distance between them, under the dipolar approximation, and, effectively, a nanostructure only interact with a few of their neighbours. Therefore, a metasurface with short scale order but long scale disorder, such as those generated for $L_c=10$ can exhibit strong SLRs despite having a large TD . This effect can also be visualised if we represent the quality factors of the SLRs in terms of the TD of the metasurfaces for both polarisation of the exciting light, figure 6. We see a decreasing trend of the quality factor in terms of TD despite outliers, such

as the metasurface generated with $L_c=10$, $S_d=0.2$ that we just commented on, and some fluctuations that we similarly explain as TD being affected by large-scale disorder while the quality factor isn't. A simple improvement would be to only define TD locally, on the scale that is relevant to the optical property dependant on the metasurfaces' disorder. However, we chose for simplicity to keep the definition of TD , equation (5), global in this work.

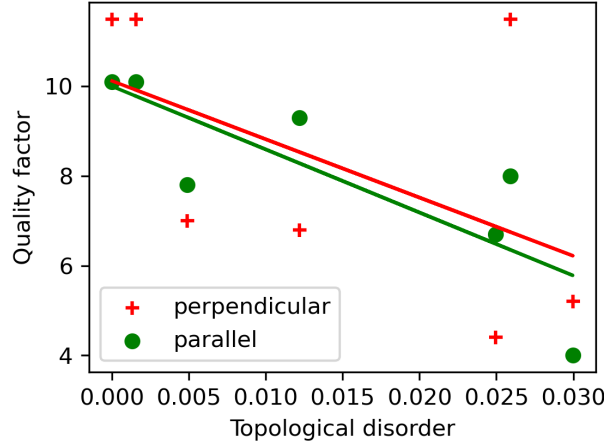


Figure 6: Graph of the quality factors of the SLRs reported in figure 5 in terms of the TD of the metasurfaces under normal incidence light linearly polarised parallel (green dots) and perpendicular (red crosses) to the long axis of the nanostructures. Two lines are added to represent the trend of the quality factors for the parallel polarisation, in green, and perpendicular polarisation, in red, in terms of TD .

This demonstrates that TD is a more accurate measure of the positional disorder of these metasurfaces compared to S_d as in all of the cases reported here, the metasurface that should have been the most ordered, generated with the lowest value of S_d , is actually at least as disordered as the metasurface that should have been the most disordered, generated with the highest value of S_d . Indeed, while a correlation length, induced by $L_c \neq 0$, made S_d more ambiguous to describe the disorder of the metasurfaces, TD was able to accurately select lattices of chosen disorder, that we experimentally probed via the quality factor of their SLRs, despite the non unique relationship between TD and SLRs quality factors.

Conclusion

We have shown how Topological Data Analysis and persistent homology can be used to classify both correlated and uncorrelated disordered metasurfaces via their topological disorder. In particular, we showed that for correlated disorder, topological disorder is a significantly more accurate measure of disorder than generative probabilistic parameters. We proved, theoretically and experimentally, this accuracy by correlating topological disorder to the strength of surface lattice resonances of metasurfaces made of plasmonic nanostructures, despite the global definition of topological disorder being sensitive to large-scale distortion, while surface lattice resonances are not. We argue that the universality, accuracy and computational speed of topological disorder makes it an advantageous tool to characterise and tune the fabrication methods of self assembled disordered metasurfaces, as well as to help design metasurfaces of specific degree of disorder, for example to enhance light extraction for more efficient LEDs or light absorption for improved solar cells.

Experimental / Method

The metasurfaces have lateral size approximately $12 \times 12 \mu\text{m}$ and were fabricated in a 50 nm thick film of Au coated glass substrate using a focused ion beam facility, Helios Nanolab 600 from FEI ThermoFisher Scientific. The metasurfaces were then spin-coated with IC1-200 whose refractive index is similar to that of the glass substrate.

The spectral characterisation was performed in transmittance at normal incidence using a microspectrophotometer (CRAIC Technologies) equipped with a tungsten-halogen light source and cooled CCD array.

The persistent homology of all lattices was computed using the Ripser python package.⁵⁰ The computation for each lattice, made of 625 nanostructures, was done in a fraction of a second. The computation of the distance between each lattice's persistence diagrams considered for the figure 3 was done using the Wasserstein distance from the GUDHI python package.⁴⁹

Embeddings were obtained from the distance matrices by using classical multidimensional scaling. We projected the embeddings in two dimensions for the visual representations in figure 3. In general such embeddings live in a very high dimensional, non necessarily euclidean, space and a projection to a two dimensional flat space can lead to distortions. However, the magnitude of these distortions can be estimated in the classical multidimensional scaling methods by considering the relative absolute value of the eigenvalues of the embedding in each dimension.⁶⁰ For the embedding represented in figure 3, the eigenvalues of the two largest dimension, used to represent the embedding in 2D, are respectively 278 and 40 time larger than the largest negative eigenvalue, proving that an embedding in an euclidean space is a good approximation. Similarly, the eigenvalues of the two largest dimension are respectively 22 and 3 times larger than the third largest positive eigenvalue, hinting that a projection in 2D is an accurate visual representation of the embedding.

The numerical simulations of the metasurfaces optical properties were done using the discrete dipole approximation⁵⁹ where each nanostructure is modelled as a dipole of the same polarisability. We assumed that the nanostructures were located in an homogeneous dielectric medium of refractive index $n = 1.41$ which is a good approximation of the refractive index of the glass substrate and of the IC1 layer. The reflectance was measured by computing the electromagnetic flux in the direction perpendicular to the surface, assuming a numerical aperture of 0.28, to match the experimental setup. The nanostructures polarisability was computed from simulating the optical response of an isolated nanostructure upon excitation by plane waves of different polarisability¹⁷, that we performed using the electromagnetic waves, frequency domain interface of the optics module of COMSOL 5.6, solved with a direct solver.⁶¹

Acknowledgement

The authors acknowledge the use of the IRIDIS High Performance Computing Facility, and associated support services at the University of Southampton, in the completion of this work. This work was supported by the Leverhulme Trust (grant RPG- 2019-055).

References

1. Chen, H.-T.; Taylor, A. J.; Yu, N. A review of metasurfaces: physics and applications. Reports on Progress in Physics **2016**, 79, 076401, Publisher: IOP Publishing.
2. Mao, P.; Liu, C.; Li, X.; Liu, M.; Chen, Q.; Han, M.; Maier, S. A.; Sargent, E. H.; Zhang, S. Single-step-fabricated disordered metasurfaces for enhanced light extraction from LEDs. Light-Science & Applications **2021**, 10, 180, Place: London Publisher: Springer Nature WOS:000694248200001.
3. Ushkov, A.; Dellea, O.; Verrier, I.; Kampfe, T.; Shcherbakov, A.; Michalon, J.-Y.; Jourlin, Y. Nanosphere Photolithography: The Influence of Nanopore Arrays Disorder on Extraordinary Optical Transmission. Photoptics: Proceedings of the 9th International Conference on Photonics, Optics and Laser Technology. Setubal, 2021; pp 46–53, WOS:000661460100006.
4. Yildirim, D. U.; Ghobadi, A.; Soydan, M. C.; Atesal, O.; Toprak, A.; Caliskan, M. D.; Ozbay, E. Disordered and Densely Packed ITO Nanorods as an Excellent Lithography-Free Optical Solar Reflector Metasurface. Acs Photonics **2019**, 6, 1812–1822, Place: Washington Publisher: Amer Chemical Soc WOS:000476684300030.
5. Wu, Z.; Zhang, Y.; Du, B.; Yang, K.; Wu, J.; Dai, T.; Dong, C.; Xia, J.; Wu, A.; Zhao, Z. Disordered metasurface-enhanced perovskite composite films with ultra-stable and wide color gamut used for backlit displays. Nano Energy **2022**, 100, 107436, Place: Amsterdam Publisher: Elsevier WOS:000811310400001.

6. Tani, T.; Hakuta, S.; Kiyoto, N.; Naya, M. Transparent near-infrared reflector metasurface with randomly dispersed silver nanodisks. Optics Express **2014**, 22, 9262–9270, Publisher: Optica Publishing Group.
7. Chen, H.; Zhao, J.; Fang, Z.; An, D.; Zhao, X. Visible Light Metasurfaces Assembled by Quasiperiodic Dendritic Cluster Sets. Advanced Materials Interfaces **2019**, 6, 1801834, Place: Hoboken Publisher: Wiley WOS:000459485500013.
8. Piechulla, P. M.; Slivina, E.; Batzner, D.; Fernandez-Corbaton, I.; Dhawan, P.; Wehrspohn, R. B.; Sprafke, A. N.; Rockstuhl, C. Antireflective Huygens' Metasurface with Correlated Disorder Made from High-Index Disks Implemented into Silicon Heterojunction Solar Cells. Acs Photonics **2021**, 8, 3476–3485, Place: Washington Publisher: Amer Chemical Soc WOS:000753681400009.
9. Shutsko, I.; Buchmueller, M.; Meudt, M.; Goernn, P. Light-Controlled Fabrication of Disordered Hyperuniform Metasurfaces. Advanced Materials Technologies **2022**, 7, 2200086, Place: Hoboken Publisher: Wiley WOS:000803023000001.
10. Piechulla, P. M.; Muehlenbein, L.; Wehrspohn, R. B.; Nanz, S.; Abass, A.; Rockstuhl, C.; Sprafke, A. Fabrication of Nearly-Hyperuniform Substrates by Tailored Disorder for Photonic Applications. Advanced Optical Materials **2018**, 6, 1701272, eprint: <https://onlinelibrary.wiley.com/doi/pdf/10.1002/adom.201701272>.
11. Narasimhan, V.; Siddique, R. H.; Park, H.; Choo, H. Bioinspired Disordered Flexible Metasurfaces for Human Tear Analysis Using Broadband Surface-Enhanced Raman Scattering. Acs Omega **2020**, 5, 12915–12922, Place: Washington Publisher: Amer Chemical Soc WOS:000541503700034.
12. Siddique, R. H.; Donie, Y. J.; Gomard, G.; Yalamanchili, S.; Merdzhanova, T.; Lemmer, U.; Hölscher, H. Bioinspired phase-separated disordered nanostructures for thin

- photovoltaic absorbers. Science Advances **2017**, 3, e1700232, Publisher: American Association for the Advancement of Science.
13. Donie, Y. J.; Schliske, S.; Siddique, R. H.; Mertens, A.; Narasimhan, V.; Schackmar, F.; Pietsch, M.; Hossain, I. M.; Hernandez-Sosa, G.; Lemmer, U.; Gomard, G. Phase-Separated Nanophotonic Structures by Inkjet Printing. Acs Nano **2021**, 15, 7305–7317, Place: Washington Publisher: Amer Chemical Soc WOS:000645436800116.
 14. Cao, H.; Eliezer, Y. Harnessing disorder for photonic device applications. Applied Physics Reviews **2022**, 9, 011309.
 15. El Shamy, E.; Jaeck, J.; Haidar, R.; Bouchon, P. Light scattering by correlated disordered assemblies of nanoantennas. Applied Physics Letters **2019**, 115, 041103, Place: Melville Publisher: Amer Inst Physics WOS:000477625500006.
 16. Antosiewicz, T. J.; Tarkowski, T. Localized Surface Plasmon Decay Pathways in Disordered Two-Dimensional Nanoparticle Arrays. ACS Photonics **2015**, 2, 1732–1738, Publisher: American Chemical Society.
 17. Sterl, F.; Herkert, E.; Both, S.; Weiss, T.; Giessen, H. Shaping the Color and Angular Appearance of Plasmonic Metasurfaces with Tailored Disorder. Acs Nano **2021**, 15, 10318–10327, Place: Washington Publisher: Amer Chemical Soc WOS:000665748900097.
 18. Chevalier, P.; Bouchon, P.; Jaeck, J.; Lauwick, D.; Bardou, N.; Kattnig, A.; Pardo, F.; Haider, R. Absorbing metasurface created by diffractionless disordered arrays of nanoantennas. Applied Physics Letters **2015**, 107, 251108, Place: Melville Publisher: Amer Inst Physics WOS:000368442100008.
 19. Zhang, H.; Cheng, Q.; Chu, H.; Christogeorgos, O.; Wu, W.; Hao, Y. Hyperuniform disordered distribution metasurface for scattering reduction. Applied Physics Letters **2021**, 118, 101601, Place: Melville Publisher: Amer Inst Physics WOS:000630491100001.

20. Haghtalab, M.; Tamagnone, M.; Zhu, A. Y.; Safavi-Naeini, S.; Capasso, F. Ultrahigh Angular Selectivity of Disorder-Engineered Metasurfaces. *Acs Photonics* **2020**, 7, 991–1000, Place: Washington Publisher: Amer Chemical Soc WOS:000526355400019.
21. Bertin, H.; Brule, Y.; Magno, G.; Lopez, T.; Gogol, P.; Pradere, L.; Gralak, B.; Barat, D.; Demesy, G.; Dagens, B. Correlated Disordered Plasmonic Nanostructures Arrays for Augmented Reality. *Acs Photonics* **2018**, 5, 2661–+, Place: Washington Publisher: Amer Chemical Soc WOS:000439532600018.
22. Sterl, F.; Strohfeldt, N.; Both, S.; Herkert, E.; Weiss, T.; Giessen, H. Design Principles for Sensitivity Optimization in Plasmonic Hydrogen Sensors. *Acs Sensors* **2020**, 5, 917–927, Place: Washington Publisher: Amer Chemical Soc WOS:000529155400005.
23. Roubaud, G.; Bondareff, P.; Volpe, G.; Gigan, S.; Bidault, S.; Gresillon, S. Far-Field Wavefront Control of Nonlinear Luminescence in Disordered Gold Metasurfaces. *Nano Letters* **2020**, 20, 3291–3298, Place: Washington Publisher: Amer Chemical Soc WOS:000535255300046.
24. Veksler, D.; Maguid, E.; Shitrit, N.; Ozeri, D.; Kleiner, V.; Hasman, E. Multiple Wavefront Shaping by Metasurface Based on Mixed Random Antenna Groups. *Acs Photonics* **2015**, 2, 661–667, Place: Washington Publisher: Amer Chemical Soc WOS:000355066900014.
25. Jang, M.; Horie, Y.; Shibukawa, A.; Brake, J.; Liu, Y.; Kamali, S. M.; Arbabi, A.; Ruan, H.; Faraon, A.; Yang, C. Wavefront shaping with disorder-engineered metasurfaces. *Nature Photonics* **2018**, 12, 84–90, Number: 2 Publisher: Nature Publishing Group.
26. Kim, W.; Simpkins, B. S.; Guo, H.; Hendrickson, J. R.; Guo, J. Hyperuniform disordered metal-insulator-metal gap plasmon metasurface near perfect light absorber. *Optical Materials Express* **2021**, 11, 4083–4092, Publisher: Optica Publishing Group.

27. Reyes-Coronado, A.; Pirruccio, G.; Gonzalez-Alcalde, A. K.; Urrutia-Anguiano, J. A.; Polanco-Mendoza, A. J.; Morales-Luna, G.; Vazquez-Estrada, O.; Rodriguez-Gomez, A.; Issa, A.; Jradi, S.; Garcia-Valenzuela, A.; Barrera, R. G. Enhancement of Light Absorption by Leaky Modes in a Random Plasmonic Metasurface. Journal of Physical Chemistry C **2022**, 126, 3163–3170, Place: Washington Publisher: Amer Chemical Soc WOS:000766228300025.
28. Jouanin, A.; Hugonin, J. P.; Lalanne, P. Designer Colloidal Layers of Disordered Plasmonic Nanoparticles for Light Extraction. Advanced Functional Materials **2016**, 26, 6215–6223, _eprint: <https://onlinelibrary.wiley.com/doi/pdf/10.1002/adfm.201600730>.
29. Bertolotti, J. Designing disorder. Nature Photonics **2018**, 12, 59–60, Number: 2 Publisher: Nature Publishing Group.
30. Rothhammer, M.; Zollfrank, C.; Busch, K.; von Freymann, G. Tailored Disorder in Photonics: Learning from Nature. Advanced Optical Materials **2021**, 9, 2100787, _eprint: <https://onlinelibrary.wiley.com/doi/pdf/10.1002/adom.202100787>.
31. Dupré, M.; Hsu, L.; Kanté, B. On the design of random metasurface based devices. Scientific Reports **2018**, 8, 7162, Number: 1 Publisher: Nature Publishing Group.
32. Yu, S.; Qiu, C.-W.; Chong, Y.; Torquato, S.; Park, N. Engineered disorder in photonics. Nature Reviews Materials **2021**, 6, 226–243, Number: 3 Publisher: Nature Publishing Group.
33. Pestourie, R.; Yao, W.; Kanté, B.; Johnson, S. G. Efficient Inverse Design of Large-Area Metasurfaces for Incoherent Light. ACS Photonics **2023**, 10, 854–860, Publisher: American Chemical Society.
34. Li, Z.; Pestourie, R.; Lin, Z.; Johnson, S. G.; Capasso, F. Empowering Metasurfaces with Inverse Design: Principles and Applications. ACS Photonics **2022**, 9, 2178–2192, Publisher: American Chemical Society.

35. Jiang, J.; Chen, M.; Fan, J. A. Deep neural networks for the evaluation and design of photonic devices. Nature Reviews Materials **2021**, 6, 679–700, Number: 8 Publisher: Nature Publishing Group.
36. Khoram, E.; Wu, Z.; Qu, Y.; Zhou, M.; Yu, Z. Graph Neural Networks for Metasurface Modeling. ACS Photonics **2023**, 10, 892–899, Publisher: American Chemical Society.
37. Hammond, A. M.; Slaby, J. B.; Probst, M. J.; Ralph, S. E. Phase-Injected Topology Optimization for Scalable and Interferometrically Robust Photonic Integrated Circuits. ACS Photonics **2023**, 10, 808–814, Publisher: American Chemical Society.
38. Ballew, C.; Roberts, G.; Zheng, T.; Faraon, A. Constraining Continuous Topology Optimizations to Discrete Solutions for Photonic Applications. ACS Photonics **2023**, 10, 836–844, Publisher: American Chemical Society.
39. Xu, M.; He, Q.; Pu, M.; Zhang, F.; Li, L.; Sang, D.; Guo, Y.; Zhang, R.; Li, X.; Ma, X.; Luo, X. Emerging Long-Range Order from a Freeform Disordered Metasurface. Advanced Materials **2022**, 34, 2108709, Place: Weinheim Publisher: Wiley-V C H Verlag Gmbh WOS:000772421000042.
40. Xu, X.; Cisewski-Kehe, J.; Green, S. B.; Nagai, D. Finding cosmic voids and filament loops using topological data analysis. Astronomy and Computing **2019**, 27, 34–52.
41. Heydenreich, S.; Brück, B.; Harnois-Déraps, J. Persistent homology in cosmic shear: Constraining parameters with topological data analysis. Astronomy & Astrophysics **2021**, 648, A74, Publisher: EDP Sciences.
42. Cramer Pedersen, M.; Robins, V.; Mortensen, K.; Kirkensgaard, J. J. K. Evolution of local motifs and topological proximity in self-assembled quasi-crystalline phases. Proceedings of the Royal Society a-Mathematical Physical and Engineering Sciences **2020**, 476, 20200170, Place: London Publisher: Royal Soc WOS:000571133900001.

43. Hiraoka, Y.; Nakamura, T.; Hirata, A.; Escobar, E. G.; Matsue, K.; Nishiura, Y. Hierarchical structures of amorphous solids characterized by persistent homology. Proceedings of the National Academy of Sciences of the United States of America **2016**, 113, 7035–7040, Place: Washington Publisher: Natl Acad Sciences WOS:000379033400037.
44. Ormrod Morley, D.; Salmon, P. S.; Wilson, M. Persistent homology in two-dimensional atomic networks. The Journal of Chemical Physics **2021**, 154, 124109, Publisher: American Institute of Physics.
45. Hirata, A.; Wada, T.; Obayashi, I.; Hiraoka, Y. Structural changes during glass formation extracted by computational homology with machine learning. Communications Materials **2020**, 1, 98, Place: London Publisher: Springer Nature WOS:000610591200004.
46. Onodera, Y.; Kohara, S.; Salmon, P. S.; Hirata, A.; Nishiyama, N.; Kitani, S.; Zeidler, A.; Shiga, M.; Masuno, A.; Inoue, H.; Tahara, S.; Polidori, A.; Fischer, H. E.; Mori, T.; Kojima, S.; Kawaji, H.; Kolesnikov, A. I.; Stone, M. B.; Tucker, M. G.; McDonnell, M. T. et al. Structure and properties of densified silica glass: characterizing the order within disorder. Npg Asia Materials **2020**, 12, 85, Place: Berlin Publisher: Nature Research WOS:000603065100002.
47. Edelsbrunner, H.; Harer, J. L. Computational Topology: An Introduction; American Mathematical Society, 2022; Google-Books-ID: LiljEAAAQBAJ.
48. Chazal, F.; Michel, B. An Introduction to Topological Data Analysis: Fundamental and Practical Aspects for Data Scientists. Frontiers in Artificial Intelligence **2021**, 4.
49. The GUDHI Project, GUDHI User and Reference Manual; GUDHI Editorial Board, 2015.
50. Bauer, U. Ripser: efficient computation of Vietoris-Rips persistence barcodes. J. Appl. Comput. Topol. **2021**, 5, 391–423.

51. Edelsbrunner, H.; Letscher, D.; Zomorodian, A. Topological persistence and simplification. *Proceedings 41st Annual Symposium on Foundations of Computer Science*. 2000; pp 454–463, ISSN: 0272-5428.
52. Wang, J. In Geometric Structure of High-Dimensional Data and Dimensionality Reduction; Wang, J., Ed.; Springer: Berlin, Heidelberg, 2012; pp 115–129.
53. Hensel, F.; Moor, M.; Rieck, B. A Survey of Topological Machine Learning Methods. Frontiers in Artificial Intelligence **2021**, 4.
54. Leykam, D.; Angelakis, D. G. Topological data analysis and machine learning. Advances in Physics: X **2023**, 8, 2202331, Publisher: Taylor & Francis _eprint: <https://doi.org/10.1080/23746149.2023.2202331>.
55. Membrillo Solis, I.; Orlova, T.; Bednarska, K.; Lesiak, P.; Woliński, T. R.; D’Alessandro, G.; Brodzki, J.; Kaczmarek, M. Tracking the time evolution of soft matter systems via topological structural heterogeneity. Communications Materials **2022**, 3, 1–11, Number: 1 Publisher: Nature Publishing Group.
56. Atienza, N.; Gonzalez-Diaz, R.; Soriano-Trigueros, M. A new entropy based summary function for topological data analysis. Electronic Notes in Discrete Mathematics **2018**, 68, 113–118.
57. He, Y.; Xia, S.; Angelakis, D. G.; Song, D.; Chen, Z.; Leykam, D. Persistent homology analysis of a generalized Aubry-Andre-Harper model. Physical Review B **2022**, 106, 054210, Place: College Pk Publisher: Amer Physical Soc WOS:000861332900001.
58. Ali, D.; Asaad, A.; Jimenez, M.-J.; Nanda, V.; Paluzo-Hidalgo, E.; Soriano-Trigueros, M. A Survey of Vectorization Methods in Topological Data Analysis. 2022; <http://arxiv.org/abs/2212.09703>, arXiv:2212.09703 [math].

59. Fradkin, I. M.; Dyakov, S. A.; Gippius, N. A. Fourier modal method for the description of nanoparticle lattices in the dipole approximation. Physical Review B **2019**, *99*, 075310.
60. Cox, T. C., Michael Multidimensional Scaling, 2nd ed.; Chapman and Hall/CRC: New York, 2000.
61. COMSOL[®] v. 5.6. www.comsol.com. COMSOL AB, Stockholm, Sweden.